

## focal point

Ji-Xin Cheng  
WELDON SCHOOL OF BIOMEDICAL ENGINEERING AND  
DEPARTMENT OF CHEMISTRY  
PURDUE UNIVERSITY  
WEST LAFAYETTE, INDIANA 47907

# Coherent Anti-Stokes Raman Scattering Microscopy

## INTRODUCTION

Breakthroughs in biology often arise from the development of new microscopy tools. Our understanding of biological systems has greatly benefited from the studies with electron microscopy, phase contrast microscopy, confocal fluorescence microscopy, scanning probe microscopy, and other imaging tools. In recent years, the coupling of nonlinear optics with scanning microscopy opened up a new window through which to watch the biological world. The tight focusing condition in microscopy allows an efficient generation of nonlinear optical (NLO) signals even with low pulse energies. Meanwhile, the nonlinear dependence on excitation intensity ensures that the NLO signal is only generated in the focal center, providing an inherent three-dimensional (3D) spatial resolution. In this sense, nonlinear optics was “born” for imaging use.

The earliest development of NLO microscopy can be traced back to the 1970s when second-harmonic imaging of crystals was reported as a

proof-of-principle of second-harmonic generation (SHG) microscopy.<sup>1,2</sup> In 1982, Duncan and co-workers reported coherent anti-Stokes Raman scattering (CARS) imaging of D<sub>2</sub>O in onion cells using a dye laser system.<sup>3</sup> However, these early papers did not prompt a lot of activity in the 1980s. The prosperity of the multiphoton and NLO microscopy field was triggered by the demonstration of two-photon excitation fluorescence (TPEF) imaging with a mode-locked femtosecond dye laser in 1990,<sup>4</sup> followed by demonstrations of high-quality third harmonic generation (THG) imaging<sup>5</sup> and CARS imaging<sup>6</sup> in the late 1990s. Nowadays, TPEF and SHG microscopy have become powerful tools for biological research.<sup>7,8</sup>

The first systematic study of the CARS phenomenon was published in 1965 by two scientists from the Ford Motor company.<sup>9</sup> CARS spectroscopy emerged in the early 1970s<sup>10</sup> and has been one of the most important coherent Raman spectroscopy techniques.<sup>11–13</sup> In a CARS process, three laser fields at the pump ( $\omega_p$ ), Stokes ( $\omega_s$ ), and probe ( $\omega_p'$ ) frequencies interact with a medium to

generate a new field at the anti-Stokes frequency  $\omega_{as} = (\omega_p - \omega_s) + \omega_p'$ . In most experiments, the pump field  $E_p$  and probe field  $E_p'$  come from the same laser beam. The CARS signal arises from the third-order-induced polarization,  $P^{(3)} = \chi^{(3)}E_pE_sE_p$ . CARS occurs in any medium with nonzero susceptibility  $\chi^{(3)}$ . Importantly, the CARS signal can be significantly enhanced when the beating frequency,  $(\omega_p - \omega_s)$ , is in resonance with a molecular vibration (Fig. 1A). By scanning  $(\omega_p - \omega_s)$ , one can acquire a CARS spectrum that carries essentially the same information as the spontaneous Raman spectrum of the same sample. However, because of the interference between the Raman component and the nonresonant component, the CARS line profile is dispersed, with a shift of the peak to lower frequency and appearance of a dip at higher frequency (Fig. 1B).

In a CARS experiment, other coherent Raman processes occur simultaneously, including coherent Stokes Raman scattering (CSRS), stimulated Raman gain (SRG), stimulated Raman loss (SRL), and Raman-induced Kerr effect (RIKE).<sup>11,14</sup>

**focal point**

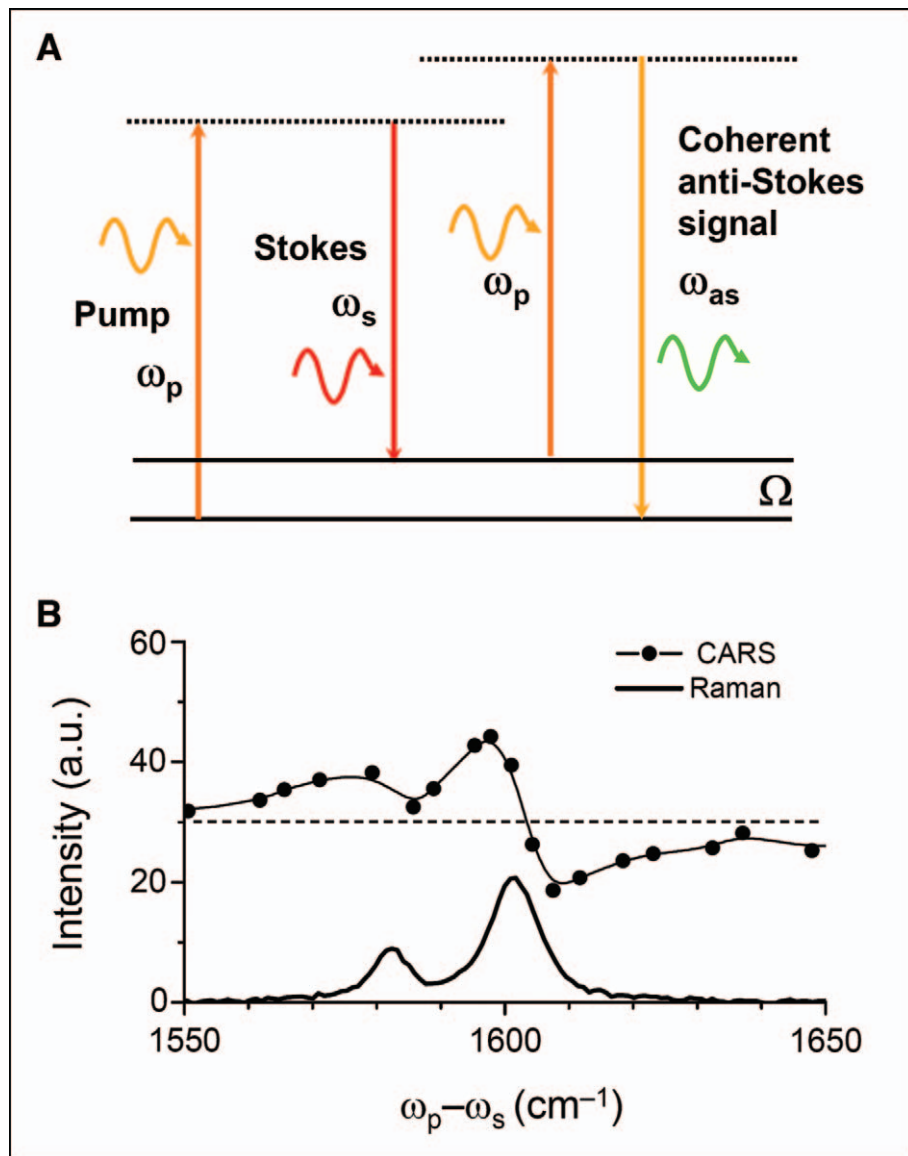


**Fig. 1.** (A) Energy diagram of CARS. (B) CARS and Raman spectra of polystyrene in the 1550 to 1650 cm<sup>-1</sup> region. The nonresonant background is indicated by the dashed line. The red shift of the CARS peaks and the dip at 1608 cm<sup>-1</sup> result from the interference between the resonant signal and the nonresonant background.

In CSRS, a new field at frequency  $\omega_s - (\omega_p - \omega_s)$  is generated. In SRG, the  $\omega_s$  field experiences a gain while in SRL the  $\omega_p$  field experiences a loss. In RIKE, new polarization components of the excitation fields are generated. In most CARS imaging experiments, two parallel-polarized beams are used, where RIKE is negligible ( $\chi_{2111} = 0$  for an isotropic medium). In contrast to SRG, SRL, and RIKE, the CARS signal is spectrally separated from the excitation

beams, making it easy to filter out the linear scattering from a heterogeneous biological system. Compared with CSRS, the CARS signal appears at a wavelength shorter than excitation wavelengths, usually in the visible region where detectors of high quantum efficiency are available.

In CARS microscopy,<sup>15-18</sup> the pump and Stokes beams are tightly focused into a sample and a CARS image is generated by scanning ei-

ther the sample or the laser beams. Besides the 3D sectioning capability, CARS microscopy offers several unique advantages.

(1) CARS microscopy permits nondestructive molecular imaging without any labeling. This advantage is important for imaging small molecules such as lipids or drugs for which the labeling may significantly affect the molecular properties.

(2) The coherent addition of CARS fields results in a quadratic signal increase with respect to the number of molecular oscillators, versus the linear increase of spontaneous Raman signal. The coherent addition also results in a highly directional output, which greatly facilitates the signal collection. The large CARS signal allows high-speed vibrational imaging, which is not possible with Raman microscopy.

(3) CARS signals appear at a wavelength that is shorter than excitation wavelengths, spectrally separated from the one-photon fluorescence background.

The major disadvantage of CARS is the existence of a nonresonant background which arises from the electronic contribution to  $\chi^{(3)}$ . This nonresonant background is coherently mixed with the vibrationally resonant signal, which limits the sensitivity of CARS in detecting weak Raman bands. Additionally, the resonant CARS signal decreases quadratically with the molecular concentration, making the detection of low-concentration molecules difficult. In the past few years, tremendous efforts have been spent on suppressing the nonresonant background and pushing the detection sensitivity limit.

This paper aims to evaluate the potential and limitations of CARS microscopy through a review of recent advances. The rest of the paper will discuss the technical developments, summarize the biological and biomedical applications, and finally present an outlook.

**TECHNICAL DEVELOPMENTS**

The first attempt toward using CARS as a microscopy technique

was made by Duncan and co-workers in the 1980s.<sup>3,19,20</sup> Using visible dye lasers, non-collinear beam geometry, and a charge-coupled device (CCD) detector to record the signal at the phase matching direction, the authors acquired CARS images of D<sub>2</sub>O distribution in onion cells. Xie and co-workers revived CARS microscopy in 1999 using near-infrared laser pulses and a collinear beam geometry.<sup>6</sup> Significant advances in the last few years have matured CARS microscopy, as summarized below.

**Construction of a Robust Coherent Anti-Stokes Raman Scattering Microscope.** The combined use of the following strategies has produced a CARS microscope for imaging highly dynamic systems with repeatable results. A schematic of such a microscope is shown in Fig. 2. It is notable that most of these strategies involved the breakdown of conventional wisdoms rooted from CARS spectroscopy.

**Near-Infrared Laser Excitation.** The use of a near-infrared laser pulse first by Zumbusch et al. avoided two-photon electronic enhancement of the nonresonant contribution.<sup>6</sup> Because the generation of CARS does not need one-photon or two-photon electronic resonance, even longer excitation wavelengths (i.e., 1.2 μm) can be used to reduce tissue scattering and increase the optical penetration depth accordingly.<sup>21</sup> The use of longer wavelengths could also reduce the photo-damage induced by multiphoton absorption.<sup>22</sup>

**Collinear Beam Geometry.** As a four-wave-mixing process, the generation of CARS needs to fulfill the phase matching condition,  $|\mathbf{k}_{as} - (2\mathbf{k}_p - \mathbf{k}_s)|L < \pi$ , where  $L$  is the light-sample interaction length.  $\mathbf{k}_p$ ,  $\mathbf{k}_s$ , and  $\mathbf{k}_{as}$  are wave vectors of the pump, Stokes, and CARS fields, respectively. With a collinear beam geometry, dispersion of the refractive index ( $n_j$ ,  $j = p, s$ , and  $as$ ) introduces a wave vector mismatch of  $(n_{as}\omega_{as} - 2n_p\omega_p + n_s\omega_s)/c$ . In order to maximize the interaction length, non-collinear beam geometries were used in CARS spectroscopy to minimize the wave vector mismatch. This method

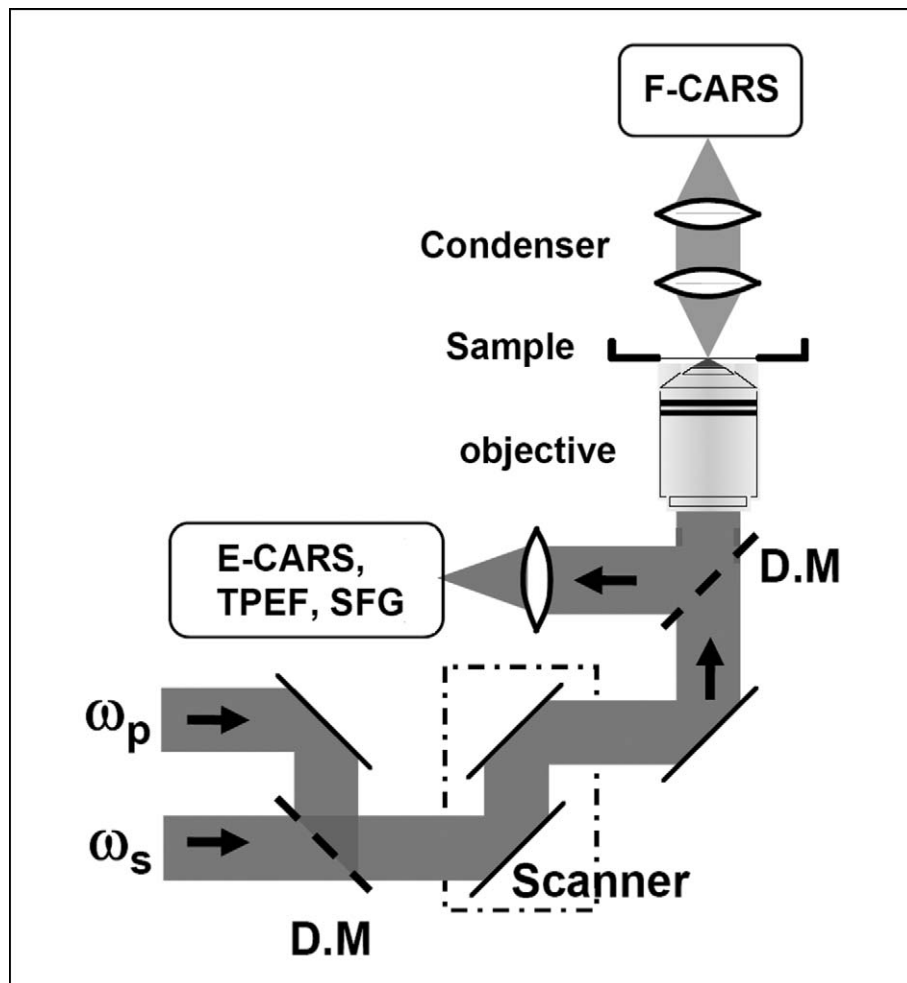


Fig. 2. Schematic of a laser-scanning CARS microscope that allows imaging with forward-detected CARS (F-CARS), epi-detected CARS (E-CARS), two-photon excitation fluorescence (TPEF), and sum frequency generation (SFG) signals produced by two synchronized pulsed lasers at frequencies  $\omega_p$  and  $\omega_s$ . D.M, dichroic mirror.

was also used in the 1982 CARS microscope.<sup>3</sup> Xie and co-workers realized that the phase mismatch could be relaxed with a tight focus using a high numerical aperture objective in microscopy.<sup>6</sup> Because the interaction length is around several micrometers or less under the tight focusing condition, the phase matching condition can be fulfilled with a collinear beam geometry for forward detection. The collinear beam geometry greatly simplified the implementation and has been a key step in producing high-quality CARS images.

**Picosecond Pulse Excitation.** It is generally valid that femtosecond pulses provide a high peak intensity that is needed for NLO processes.

However, this wisdom becomes invalid in CARS microscopy.<sup>23</sup> In the spectral domain, the spectral width of a femtosecond pulse is much broader than the width of most Raman lines. As a result, most of the energy only contributes to the generation of nonresonant background. Instead, the spectral width of a picosecond pulse matches the Raman line width, so that the excitation energy can be focused on a single Raman band. Thus, the use of picosecond pulse excitation not only provides sufficient spectral resolution,<sup>24</sup> but also increases the ratio of resonant signal to non-resonant background.<sup>23</sup> Currently picosecond pulse excitation can be realized by using

## focal point

two synchronized Ti:sapphire lasers<sup>23</sup> or using an optical parametric oscillator pumped by a pulsed laser.<sup>21,25</sup>

**Epi- (i.e., Backward-) Detection.** For isotropic bulk samples studied in CARS spectroscopy, the signal goes forward in the phase matching direction. Unlike spectroscopy, microscopy studies heterogeneous samples. For objects that are much smaller than the excitation wavelengths, the phase matching condition is relaxed and the CARS radiation pattern becomes symmetrical forward and backward.<sup>23,26</sup> Systematic study showed that epi-detected CARS (E-CARS) could arise from objects of small interaction length, discontinuity of  $\chi^{(3)}$  at an interface, and back-reflection of forward CARS.<sup>27</sup> Because the CARS signal from the surrounding solvent goes forward, E-CARS provided a means to detect small objects embedded in a bulk medium.<sup>23,26</sup> Another significant application of E-CARS is live animal imaging for which it is impossible for the forward CARS signal to pass through a thick tissue.<sup>28,29</sup>

**Laser Scanning.** In early papers, CARS images were generated by using low repetition rate (in KHz) pulses that had a high peak power in order to ensure a large signal level. However, the use of low repetition rate pulses necessitated minutes for recording an image on a sample scanning platform, which was not suitable for live cell or *in vivo* imaging. Later, using a confocal microscope (Olympus, FV300/IX71), it was shown that the same sensitivity could be achieved by scanning picosecond lasers of high repetition rates (in MHz), with an image acquisition speed of a frame per second.<sup>30</sup> More recently, video-rate scanning CARS has been demonstrated.<sup>28</sup> The implementation of CARS imaging on a laser-scanning microscope platform not only ensures high-speed imaging of highly dynamic systems, but also makes CARS microscopy compatible with a common confocal fluorescence microscope and other NLO imaging modalities. Similar to TPEF micros-

copy, the confocal pinhole is not used for laser-scanning CARS imaging. Additionally, non-descanned large area detectors can be used to increase the detection sensitivity for tissue imaging. A major difference between CARS and TPEF is that CARS utilizes two excitation laser beams at different wavelengths. Therefore, microscope objectives with minimal chromatic aberrations should be used to ensure effective signal generation as well as collection.

**Suppression of Nonresonant Background.** For fingerprint Raman bands such as the amide I band, the resonant CARS signal could be buried in the large nonresonant background from the object of interest as well as the surrounding medium. Several strategies were used to improve the signal to background ratio in CARS spectroscopy, including polarization-sensitive detection,<sup>31,32</sup> time-resolved detection,<sup>33</sup> electronic resonance excitation,<sup>34,35</sup> and interferometry.<sup>36</sup> Except for resonance CARS, which may induce serious damage under the tight focusing condition, these methods have been demonstrated on the microscope platform for background-free vibrational imaging, as summarized below.

**Polarization-Sensitive Detection.** Polarization-sensitive detection<sup>37,38</sup> utilizes the different polarization properties of the resonant and nonresonant components of  $\chi^{(3)}$ . Away from one-photon electronic resonance, the depolarization ratio of the nonresonant CARS field equals 1/3 following the Kleinman's symmetry.<sup>39</sup> The depolarization ratio of the resonant CARS field equals the Raman depolarization ratio and varies in the range of 0 to 0.75. The nonresonant background can be rejected by placing an analyzer before the detector while a projection of the resonant signal along the analyzer polarization can be detected.

**Time-Resolved Detection.** Time-resolved detection<sup>40</sup> makes use of the different free-induction decay rates of the resonant and nonresonant contributions. With a flat profile in the

spectral domain, the nonresonant background contributes to an instantaneous spike in the time domain due to electronic dephasing. The resonant part involves a vibrational transition and has a longer dephasing time (on the order of one picosecond) that is related to the spectral width of the corresponding Raman line. Thus, the nonresonant background can be eliminated by introducing a suitable time delay between the femtosecond pump/Stokes pulses and the probe pulse.

**Spectral and Spatial Phase Control.** In spectral phase control,<sup>41,42</sup> the pulse shaping technique was applied to modulate the phase of different spectral components in a femtosecond pulse with a periodic function (period  $\Omega_m$ ). As a result, a Raman-resonant signal with vibrational frequency of  $N\Omega_m$  ( $N$  is an integer) gets constructive interference, while the nonresonant signal is canceled by destructive interference. This method allowed CARS imaging with a single femtosecond beam.<sup>41</sup> Recently, spatial phase shaping of focus was implemented to cancel the coherent addition of the nonresonant signal from a bulk medium, which permitted the visualization of interfaces.<sup>43,44</sup> It should be noted that the nonresonant signal from bulk solvent can also be canceled by using counter-propagating pump and Stokes laser beams to introduce a large spatial phase mismatch inside the focal volume.<sup>27</sup>

**Interferometric Coherent Anti-Stokes Raman Scattering.** Interferometric coherent anti-Stokes Raman scattering<sup>45-52</sup> separates the real and imaginary parts of  $\chi^{(3)}$  by using a local oscillator to interfere with the CARS signal from a sample. Moreover, this approach amplifies the signal level because the detected signal is the interference term between the resonant signal and the local oscillator.

Despite nice proof-of-principle demonstrations using standard samples such as polymer beads or solvents, the complexity of these advanced techniques may hamper their use as an analytical tool to study real

tissue samples in which the laser intensity, phase, and polarization can be significantly changed. Time-resolved detection is not affected by tissue scattering, but its ultimate sensitivity is limited by the use of femtosecond pulses, which increases the nonresonant background in the first place.

The simplest and most robust method for background removal is to digitally subtract the off-resonance CARS image from the on-resonance one. This method was first used by Duncan et al. in CARS imaging of deuterated liposomes.<sup>20</sup> By comparing the difference between the two images acquired at the peak and dip positions of a CARS band, quantitative detection of a specific deuterated lipid in a single bilayer was recently demonstrated.<sup>53</sup> To facilitate the study of more dynamic systems, the on- and off-resonance signals can be acquired simultaneously or in a frequency modulation manner by using three pulsed lasers.<sup>21,25</sup>

For C–H stretch vibrations, the Raman-resonance enhancement of  $\chi^{(3)}$  is significant because of the high density of C–H bonds in biological molecules, particularly in lipids. A resonant signal to nonresonant background ratio of more than 10:1 was obtained through multiplex CARS spectral analysis of multilamellar lipid membranes.<sup>38</sup> With the large signal from C–H vibration, CARS imaging of lipid bodies,<sup>28,54–56</sup> single cell membranes,<sup>30,57</sup> myelin sheath in central and peripheral nervous systems,<sup>29,58</sup> and drug molecules<sup>59</sup> has been demonstrated. Virtually no sophisticated background reduction schemes are needed for imaging C–H abundant objects.

**Improving the Detection Sensitivity.** In CARS, the coherent addition of anti-Stokes Raman scattering photons results in a large and directional signal. For a bulk liquid, the CARS signal was estimated to be larger than the spontaneous Raman signal by nine orders of magnitude.<sup>12</sup> Thus, CARS microscopy is naturally sensitive to molecular assemblies such as lipid membranes. On the other hand, the resonant CARS signal

drops quadratically with the reduction of the concentration of target molecules and can be buried in the nonresonant background. The sensitivity of CARS microscopy was significantly improved by using picosecond pulse excitation to focus all the energy on a single Raman band.<sup>23</sup> The use of epi-detection to reject the solvent background allowed detection of 100 nm polystyrene bead that contains  $10^6$  aromatic C–H oscillators.<sup>30</sup> The sensitivity of epi-detection was further enhanced by mixing the epi-scattered resonant CARS field with the back-reflected nonresonant CARS field.<sup>57</sup> For a d62-DPPC bilayer supported by a cover glass, such coherent mixing caused a highly dispersed spectral profile superimposed on a flat nonresonant background. By measuring the E-CARS intensity acquired at the peak and dip frequencies, Li et al. was able to probe 10% d62-DPPC in a single bilayer,<sup>53</sup> which corresponded to  $2 \times 10^4$  DPPC molecules inside the focal area of  $0.25 \mu\text{m}^2$ .

For forward detection, frequency-modulation CARS allowed the detection of  $5 \times 10^5$  methanol molecules in the excitation volume of 0.1 fL, where the CARS intensities on- and off-resonance with the  $\text{CH}_3$  stretch vibration were used.<sup>60</sup> It is worth noting that the detection sensitivity depends on the target molecule and the vibrational mode as well. For CARS imaging of natural paclitaxel molecules, the forward CARS signal from the aromatic CH vibration was used for detecting paclitaxel dissolved in *N,N*-dimethylformamide solution. The detection limit was 1.8 attomole paclitaxel in the excitation volume of 0.06 fL, corresponding to 29 mM.<sup>59</sup> Such a sensitivity allowed imaging of paclitaxel dispersed in a polymer film<sup>59</sup> but is still inadequate for imaging the drug distribution inside of a paclitaxel-treated mammalian cell.

**Multimodal Nonlinear Optical Imaging on a Coherent Anti-Stokes Raman Scattering Microscope.** Multimodality is important because different NLO imaging methods each have their distinctive

advantages: TPEF can be used to visualize proteins, ions with fluorescent labeling or specific auto-fluorescent structures; SHG and sum-frequency generation (SFG) are selective to non-centrosymmetric molecular assemblies such as collagen fibrils; and CARS is naturally sensitive to lipid-enriched structures such as adipocytes. Fu et al. realized that the two picosecond laser beams for CARS imaging could also be used for electronic SFG imaging.<sup>61</sup> The authors demonstrated multimodal NLO imaging of *ex vivo* spinal tissues by CARS imaging of myelin sheath, SFG imaging of astrocyte processes, and TPEF imaging of calcium indicators on the same platform.<sup>61</sup> At the single cell level, Nan et al. combined CARS with TPEF to characterize the relationship between lipid droplets and mitochondria.<sup>55</sup> Multimodal NLO imaging has recently been used to map the molecular composition of atheroma<sup>62</sup> and to evaluate the impact of obesity on adipocyte size and collagen fibril density in mammary tumor stroma.<sup>56</sup>

**Integrating Coherent Anti-Stokes Raman Scattering Microscopy with Spectroscopy.** Spectral analysis provides important information that is not available in a single-frequency CARS image. The high-speed imaging on a laser-scanning CARS microscope was achieved by using picosecond pulses to focus all the excitation power on a single Raman band. In this configuration, a CARS spectrum has to be recorded in a time-consuming manner by tuning the Stokes laser frequency point by point. The past few years saw a great interest in the development of multiplex CARS microscopy and microspectroscopy with pico/femto excitation,<sup>38,63</sup> chirped pulse,<sup>64,65</sup> fiber-based super-continuum,<sup>66–70</sup> and single broadband pulses.<sup>41,48,71</sup> Recently hyper-Raman microspectroscopy has also been coupled with CARS imaging using picosecond pulses.<sup>72</sup>

Multiplex CARS microscopy is usually implemented by raster-scanning a sample with a pixel dwell time on the order of milliseconds,

## focal point

limiting its application to dynamic biological systems. On the other hand, if one only needs to record the spectrum at a point of interest, microspectrometry can be implemented with the point-scan mode of a laser-scanning microscope,<sup>62</sup> where high-speed imaging and spectral recording could be obtained from the same sample. It should be noted that interpretation of CARS spectra is complicated by the nonresonant background. Recently, the maximum entropy method was successfully used to fit the CARS spectra and extract the imaginary part of the susceptibility without prior knowledge of the sample composition.<sup>73</sup>

**In Vivo Coherent Anti-Stokes Raman Scattering Imaging.** In comparison to imaging of cultured cells or extracted tissues, *in vivo* optical imaging provides a much better means to monitor cells over time without significant change or perturbation of their environment. CARS microscopy allows label-free molecular imaging. This advantage is particularly important for *in vivo* studies for which the labeling is complicated by inefficient diffusion and non-specific binding in the tissue environment. Evans et al. demonstrated E-CARS imaging of sebaceous glands, corneocytes, and adipocytes in the skin of a live mouse.<sup>28</sup> By using minimal surgery to cut open the skin, Huff et al. demonstrated *in vivo* E-CARS imaging of sciatic nerve and surrounding adipocytes.<sup>29</sup> The contrast mechanisms for *in vivo* CARS have been carefully investigated. The E-CARS signals from the sciatic nerve tissues were found to arise from interfaces as well as back reflection of forward CARS. For the densely packed skin tissue, the forward-propagating photons would experience a significantly greater number of scattering events. The skin could also distort the point spread function at the foci,<sup>74</sup> which eliminates the E-CARS signal from interfaces. In such a case, multiple reflection of forward CARS becomes the major source of E-CARS.<sup>28</sup>

### Analysis and Interpretation of a Coherent Anti-Stokes Raman

**Scattering Image.** The quantitative information that can be extracted from a CARS image is the intensity at each pixel. Converting the CARS intensity into the information of molecular composition is, however, not straightforward because of the nonresonant background that depends on the sample property at each pixel. Only in well-defined samples such as supported lipid bilayers was quantitative CARS imaging demonstrated.<sup>53</sup> Because the generation of CARS critically depends on the tight overlap of the pump and Stokes laser foci, it is suggested to routinely check the spatial overlap of the two laser beams using the transmission channel of the microscope. Calibration of the system using the nonresonant signal from a standard sample such as a cover glass is also recommended when recording a CARS spectrum or quantitatively comparing the CARS intensities between different samples. It is important to mention that for a complex biological sample, the tightness of the foci may be deteriorated by objects in the focusing path. For instance, when the foci were above a lipid droplet, the forward CARS signal was significantly reduced and a dark hole was observed in the image.<sup>30</sup> For the same reason, the efficiency of CARS generation also highly depends on the optical penetration depth. Thus, careful attention must be paid when interpreting the depth intensity profile.

The CARS intensity is also affected by the interference of two adjacent Raman bands. For this reason, when parallel-polarized pump and Stokes beams were used, the CARS peak for the symmetric CH<sub>2</sub> stretch vibration was much more pronounced than that for the asymmetric CH<sub>2</sub> vibration in lipids.<sup>38</sup> Special attention should be paid to the CARS signal from OH vibration, which was shown to be 40 times smaller than that from CH vibration.<sup>75</sup> In liposomes, the CARS contrast at 3200 cm<sup>-1</sup>, originally assigned to the interlamellar water,<sup>76</sup> was later shown to be overwhelmed by the destructive interference term between the

CH vibration and the nonresonant background.<sup>77</sup>

The dependence of CARS intensity on excitation beam polarization provides a means to determine the orientation of the oscillators. For the symmetric CH<sub>2</sub> stretch vibration, the CARS intensity is maximized when the excitation beams are polarized along the dipole of the CH<sub>2</sub> group.<sup>57,76</sup> This method has been used to determine the ordering degree of lipids in myelin sheath,<sup>58</sup> where standard samples were used to calibrate the microscope response to different excitation polarization. For a homogeneous sample, the CARS signal was shown to be linearly polarized along the excitation laser polarization.<sup>37</sup> In contrast, the CARS polarization was significantly scrambled when generated from a tissue sample.<sup>58</sup>

### Cell and Tissue Damage During Coherent Anti-Stokes Raman Scattering Imaging.

In general, because CARS does not need one-photon or two-photon electronic resonance, multi-photon absorption induced damage is diminished in CARS microscopy with near-infrared picosecond pulse excitation. Nondestructive CARS imaging of live cells over a period of 300 s has been demonstrated.<sup>55</sup> The mechanisms underlying the photo-damage in CARS microscopy have been studied using high excitation power and scanning over a small area.<sup>22,55</sup> The damage to cultured cells was found to be nonlinear, featured by cell membrane blebbing<sup>22</sup> or cell retraction.<sup>55</sup> The damage to compact myelin sheath involved both linear and nonlinear mechanisms, depending on the peak power and pulse repetition rate applied.<sup>22</sup> It was also found that the damage mainly arose from the pump laser beam, which has a shorter laser wavelength.<sup>22</sup> Therefore, the use of a higher ratio of Stokes to pump power or longer excitation wavelengths helps the reduction of damage. Besides linear and nonlinear absorption of the incident photons, an extra source of photo-damage during CARS imaging arises from vibrational excita-

tion. Theoretical analysis by Wang et al. showed that such vibrational excitation is due to the concomitant Raman gain and Raman loss processes, which contribute to an efficient light-matter energy transfer under the tight focusing condition.<sup>78</sup>

### BIOLOGICAL AND BIOMEDICAL APPLICATIONS

The ultimate goal of developing CARS microscopy is to use it as an imaging tool to address scientific questions. Encouragingly, the number of application publications is rising and several significant applications to biology and medicine have been demonstrated, as summarized below.

**Lipid Domains in Model Membranes.** Lateral heterogeneity of lipid distribution in biological membranes plays a critical role in signal transduction, membrane traffic, and diseases.<sup>79</sup> Using the CARS signal from the CH<sub>2</sub> stretch vibration, detection of single bilayers was demonstrated.<sup>57,80</sup> Potma et al. showed CARS imaging of lipid domains in giant unilamellar vesicles.<sup>81</sup> Li et al. demonstrated quantitative E-CARS imaging of specific lipids in a supported bilayer.<sup>53</sup> Molecular specificity was achieved by using lipids with deuterated acyl chains (i.e., d62-DPPC). The effect of deuteration on phase segregation was explored by comparing d62-DPPC-containing and DPPC-containing bilayers, with the same domain patterns being observed.<sup>53</sup> An example of using E-CARS to study lipid domains is described below.

The E-CARS spectrum for the CD<sub>2</sub> stretch vibration band of a single supported d62-DPPC bilayer is shown in Fig. 3A. Coherent mixing of the resonant signal from the bilayer and the non-resonant signal from the glass-water interface resulted in a peak at 2080 cm<sup>-1</sup> and a dip at 2125 cm<sup>-1</sup>. The nonresonant background was removed by subtracting the dip CARS intensity from the peak CARS intensity. The (peak - dip) signal contained the cross term between the resonant and nonresonant CARS fields, which enhanced

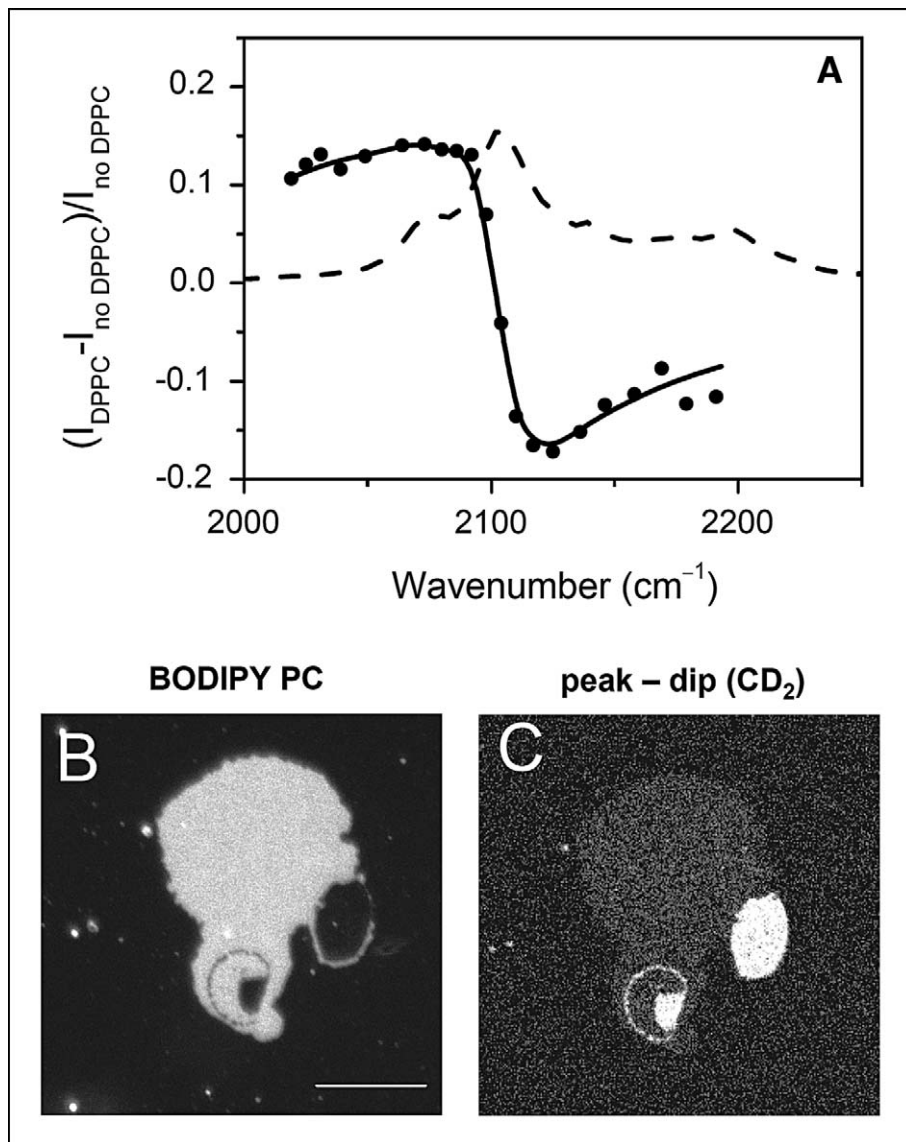


**Fig. 3. E-CARS imaging of lipid domains in a supported bilayer.** (A) E-CARS spectral profile (solid line with solid circles) of a single supported bilayer of d62-DPPC in the C-D stretch vibration region. The peak and dip of the CARS band appeared at 2080 cm<sup>-1</sup> and 2125 cm<sup>-1</sup>, respectively. The Raman spectrum (dashed line) of bulk d62-DPPC is also shown as a reference. (B) Fluorescence image of a DOPC/d62-DPPC (1:1) bilayer patch. Image was acquired at 23 °C. The liquid phase was labeled by BODIPY PC. (C) The (peak - dip) CARS image of the same sample, obtained by subtracting the CARS image at 2125 cm<sup>-1</sup> from that at 2080 cm<sup>-1</sup>. The gel phase that is enriched in d62-DPPC exhibited a bright CARS contrast. Bar length = 10 μm. Data adapted from the paper by Li et al.<sup>53</sup>

the detection sensitivity. As a result, a clear vibrational contrast was obtained from 10% d62-DPPC in a single bilayer. Moreover, Li et al. developed a theoretical model to convert the (peak - dip) intensity into molecular concentration.<sup>53</sup> These ef-

forts allowed quantitative measurement of the partition of d62-DPPC between coexisting domains, as shown in Figs. 3B and 3C. In summary, the ability to probe molecular compositions of lipid domains makes CARS microscopy a useful

## focal point

tool for the study of membrane organization.

**Cellular Analysis.** Laser-scanning CARS microscopy has been applied to vibrational imaging of cellular processes. By line-scanning the laser beams and using the resonant CARS signal from water, Potma et al. measured the intracellular water diffusion coefficient.<sup>82</sup> By using a laser-scanning CARS microscope with simultaneous forward and backward detection, Cheng et al. characterized the morphology of mitosis and apoptosis in unstained NIH3T3 cells.<sup>30</sup> Of all the cellular organelles, the lipid droplets produce the strongest CARS signal at the frequency of the C–H stretch vibration. Using the CARS signal, Nan et al. monitored adipogenesis in 3T3-L1 cells and also explored intracellular trafficking of lipid droplets in Y-1 cells.<sup>54,55</sup> These studies showed the potential of CARS microscopy in characterization of 3D cell morphology as well as the study of intracellular lipid bodies.

**Myelin Sheath and Demyelination.** The myelin sheath, an extended plasma membrane wrapping around an axon, is crucial for high-speed impulse conduction. Numerous neurological diseases specifically attack the myelin sheath with disabling and often fatal results.<sup>83</sup> The lamellar structure of myelin sheath has been well characterized by polarized light microscopy, electron microscopy, and X-ray diffraction. However, visualizing intact myelin in live tissues and *in vivo* cannot be accessed with these techniques.

The myelin membrane contains a high lipid to protein ratio with 70% lipid and 30% protein by weight. Wang et al. demonstrated CARS imaging of intact myelin sheath using the resonant CARS signal from the high-density CH<sub>2</sub> groups in the myelin membrane.<sup>58</sup> In their work, the spinal cord white matter strips were isolated from guinea pigs as illustrated in Fig. 4A. The CARS spectrum of a single axonal myelin is shown in Fig. 4B. The peak for the symmetric CH<sub>2</sub> stretch vibration appeared at 2840 cm<sup>-1</sup>, with a resonant

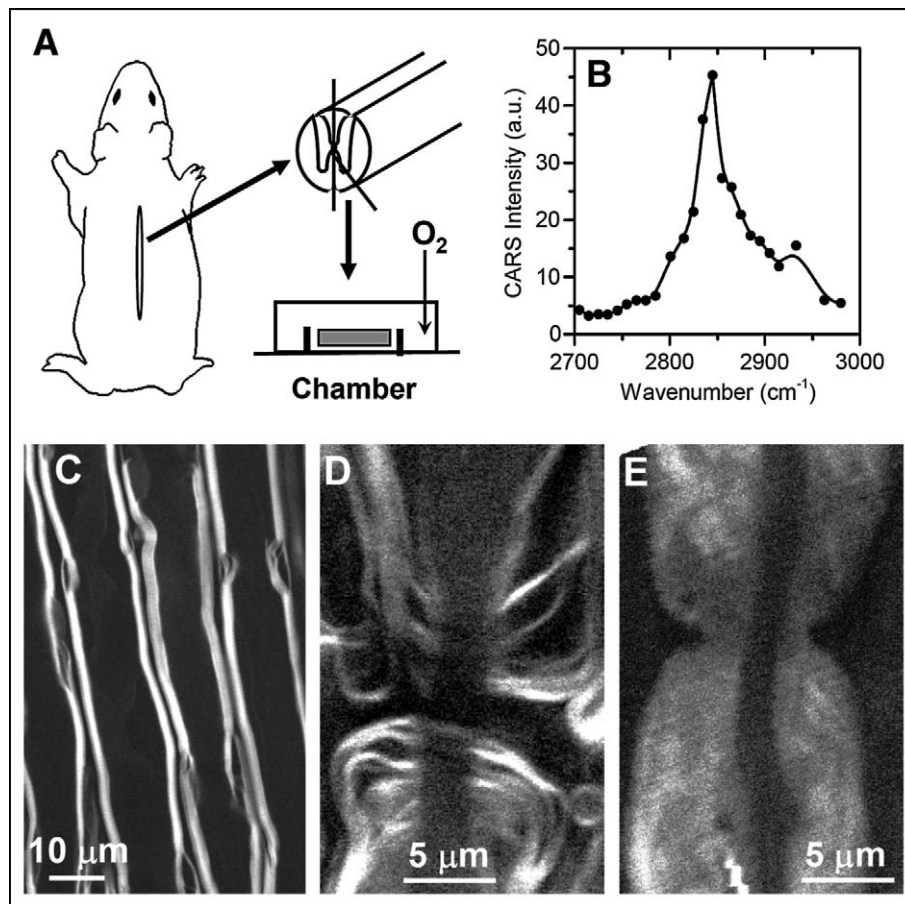


**Fig. 4.** CARS imaging of intact myelin sheath. (A) Schematic showing the procedure of extracting spinal cord white matter from a guinea pig. (B) CARS spectral profile of myelin. (C) Forward detected CARS (F-CARS) image of myelin sheath surrounding parallel axons in an ex vivo spinal tissue. (D) F-CARS image of a node of Ranvier. (E) F-CARS image of nodal myelin swelling induced by lysophosphatidylcholine. For all images,  $(\omega_p - \omega_s)$  was tuned to 2845 cm<sup>-1</sup>.

signal to nonresonant background ratio of 10:1. Additionally, a weak band at 2930 cm<sup>-1</sup> was observed and assigned to the CH<sub>3</sub> stretch mode of the myelin proteins. CARS images of myelin sheath surrounding the parallel axons and myelin around a node of Ranvier are shown in Figs. 4C and 4D, respectively. Importantly, the CARS intensity strongly depends on the excitation polarization because of the lamellar structure of the myelin membranes. Such polarization dependence as well as the CARS intensity provides means to distinguish healthy myelin from degraded myelin. Upon the treatment of lysophosphatidylcholine, a widely used demyelination agent, the myelin became swelled (Fig. 4E), char-

acterized by a three-fold decrease of CARS intensity and loss of polarization dependence.<sup>84</sup> These capabilities open up exciting opportunities to the pathological study of demyelinating diseases such as multiple sclerosis.

**Native Drug Molecules in a Polymeric Delivery System.** Visualization of three-dimensional distribution of drug molecules and subsequent changes during the release process is critical for understanding drug delivery mechanisms as well as designing tailor-made release profiles. Kang et al. demonstrated that CARS microscopy could be effectively utilized to examine paclitaxel distribution in various polymer films with lateral resolution of 0.3 μm and

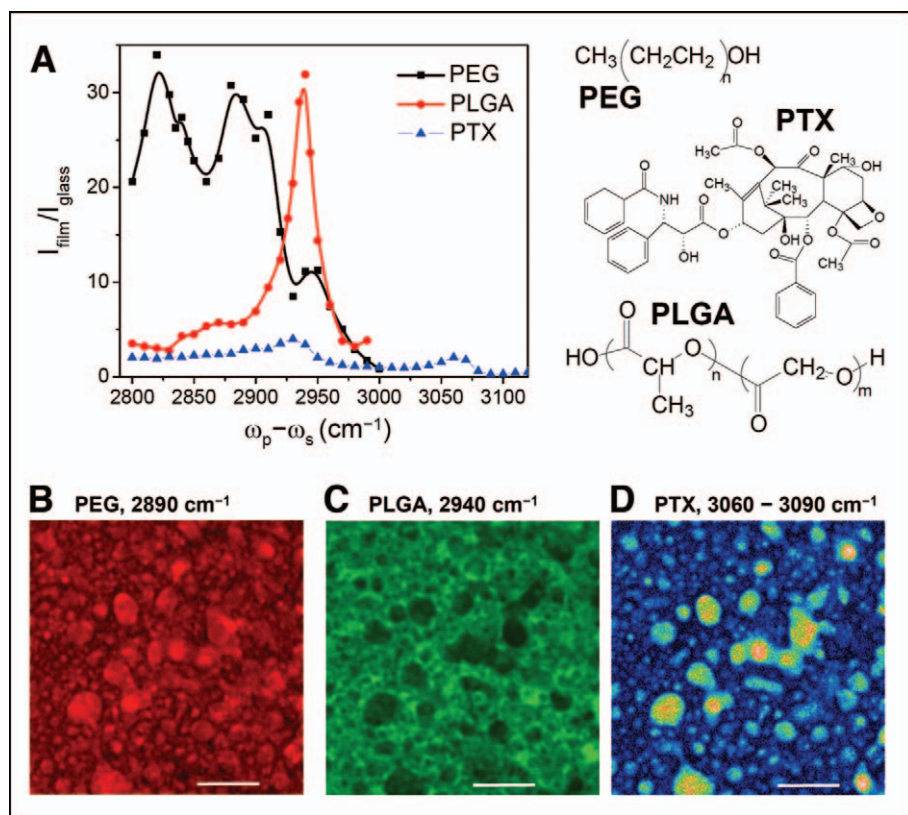


**FIG. 5.** CARS imaging of paclitaxel (PTX) distribution in a PEG/PLGA blend film. (A) CARS spectral profiles of PEG, PLGA, and PTX in the CH stretch vibration region. The molecular structures are shown on the right side. (B, C) Distribution of PEG and PLGA based on the CARS signals from CH<sub>2</sub>, CH<sub>3</sub>, and aromatic CH vibration bands, respectively. (D) PTX distribution. Image was obtained by subtracting the CARS image at 3090 cm<sup>-1</sup> from that at 3060 cm<sup>-1</sup>. Bar = 5 μm. Data adapted from the paper by Kang et al.<sup>85</sup>

depth resolution of 0.9 μm.<sup>59</sup> In a more recent study, Kang et al. studied the distribution of paclitaxel in the blend of poly(ethylene glycol)/poly(lactide-co-glycolic acid) (PEG/PLGA).<sup>85</sup> As shown in Fig. 5A, CARS signals from the aromatic CH, CH<sub>2</sub>, and CH<sub>3</sub> stretch vibration bands allowed selective imaging of paclitaxel, PEG, and PLGA.<sup>85</sup> CARS imaging revealed that PTX preferentially partitioned into the PEG domains in the phase-segregated PLGA/PEG film (Figs. 5B–5D). This result provided the first visual evidence of PTX dissolution in the PEG matrix. The re-distribution of PTX inside the films during the release process was also visualized by time-lapse CARS microscopy.<sup>85</sup> These studies demonstrate the potential of CARS micros-

copy in drug delivery formulation research.

**Obesity and Cardiovascular Disease.** With a strong signal from lipid bodies that are enriched in C–H bonds, CARS microscopy allowed selective imaging of adipocytes *in vivo*.<sup>28,29</sup> By integrating TPEF and SHG imaging modalities into a CARS microscope, Le et al. demonstrated label-free molecular imaging of atheroma induced by a high-fat diet.<sup>62</sup> As shown in Fig. 6, an atherosclerotic plaque in an iliac artery was identified by the strong CARS signal from lipids. The lipid core also showed a two-photon autofluorescence signal, but a lack of collagen fibrils based on SFG imaging results. The observed degradation of collagen fibrils is consistent with the

increased activity of matrix metalloproteinases in an atheroma.<sup>86</sup> Multi-modal NLO imaging was also utilized to evaluate the impact of obesity on molecular composition of mammary tumors in a rat model,<sup>56</sup> where obesity was found to increase the diameter of adipocytes by two-fold and collagen fibril content by five-fold. These studies showcase the potential of NLO microscopy in understanding the impact of obesity on cancer and cardiovascular disease.

**Skin and Cosmetics.** The skin is the largest organ of the body and is an important target of the cosmetics industry. CARS imaging of skin in a hairless mouse ear has been demonstrated on a video-rate scanning microscope.<sup>28</sup> The resonant CARS signal for the CH<sub>2</sub> stretch vibration allowed the visualization of polygonal corneocytes in stratum corneum,<sup>87</sup> sebaceous gland, and adipocytes within the depth of ~100 μm underneath the skin surface.<sup>28</sup> In combination with TPEF imaging of elastin and SFG imaging of collagen,<sup>88</sup> one should be able to visualize both cells and extracellular matrix in the skin tissue. These capabilities promise to provide new knowledge about skin and to help evaluate the efficacy of cosmetic agents.

## OUTLOOK FOR COHERENT ANTI-STOKES RAMAN SCATTERING MICROSCOPY

With chemical selectivity, inherent 3D resolution, and capability for high-speed data acquisition, CARS microscopy is poised to become a potent tool for biological imaging. Additionally, the ability to couple CARS with other modalities such as TPEF, SFG, and electrophysiological recording provides a powerful multimodal platform to spread the range of applications. Although biomedical applications of CARS microscopy are still in their infancy, initial works have shown great potential for this technique in medicine, especially in understanding the roles of lipids in health and diseases. One area of high impact would be obesity and associated health risks. Obesity is reaching epidemic proportions worldwide

## focal point

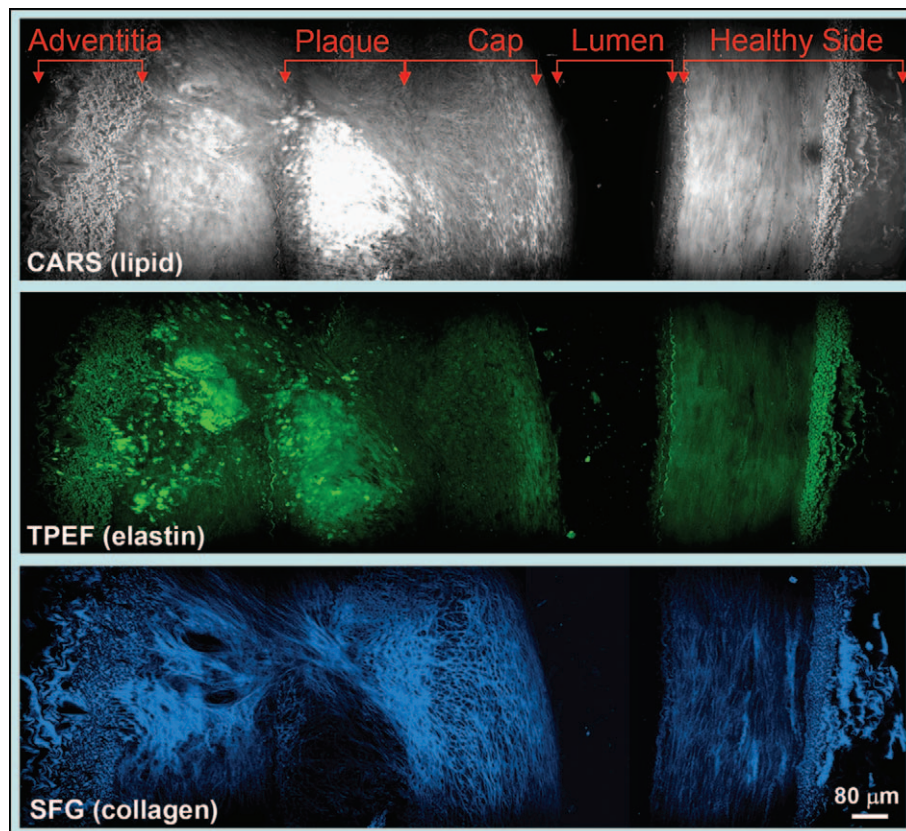


**FIG. 6.** Cross-section view of an atherosclerotic plaque in an iliac artery imaged by (top) E-CARS, (middle) TPEF, and (bottom) SFG on the same platform. The plaque is enriched in lipids (grey) and elastin (green) but devoid of collagen fibrils (blue).

and is associated with an increased risk of premature death<sup>89</sup> and cardiovascular diseases.<sup>90</sup> CARS is extremely sensitive to lipid bodies that are enriched in triglyceride.<sup>54</sup> This capability can be used to study adipogenesis in single cells<sup>91</sup> and dietary fat absorption in the intestine. Multimodal CARS microscopy has been used to evaluate the impact of obesity on mammary tumor stroma composition<sup>56</sup> and to map the composition of atheroma induced by a high-fat diet.<sup>62</sup> Another high-impact area lies in *ex vivo* and *in vivo* imaging of the nervous system, where the abundant lipids exist in the form of myelin sheath. The large and polarization-dependent CARS signal from the lamellar myelin membrane<sup>58</sup> opens up a new avenue to the study of multiple sclerosis,<sup>84</sup> a human demyelinating disease that affects 2.5 million people worldwide. Other important systems include

polymer materials, drug delivery systems, skin, and cosmetic materials. Additionally, CARS microscopy has shown unique advantages for biophysical study of lipid membrane organization.<sup>53,81,92</sup> Along with the above areas, in which CARS microscopy has shown great promise, the applications of CARS imaging are expected to continue to grow during the years to come. For instance, development of CARS probes would be attractive because they do not undergo photobleaching with proper laser power.<sup>93</sup>

The availability of an affordable, easy-to-operate multimodal CARS microscope will accelerate the development of new applications. A prohibitive factor in CARS imaging remains the cost and complexity associated with synchronizing two pulsed lasers and coupling them into a scanning microscope. The development of compact, cost-effective

laser sources and alternatives to free-space coupling such as by fiber delivery<sup>94</sup> will make the CARS imaging system more attractive to researchers in biological and biomedical areas. Meanwhile, there is still a vast amount of space for pushing the fundamental limits of the technique, e.g., increasing the sensitivity by surface-enhanced CARS,<sup>95</sup> the spatial resolution by near-field CARS,<sup>96</sup> and the imaging speed by wide-field CARS microscopy.<sup>97</sup>

One area in which CARS will prove greatly useful would be label-free *in vivo* imaging of live animals. Cellular structure and functions are best preserved in the *in vivo* environment. *In vivo* imaging also avoids trauma injuries to the tissue during the extraction process. As magnetic resonance imaging lacks single-cell resolution, *in vivo* CARS imaging will fill an important niche for study of disease processes. Although *in vivo* CARS imaging of skin tissues<sup>28</sup> and peripheral nerves<sup>29</sup> has been demonstrated, several technical hurdles such as minimizing surgery, compensating for animal motion, and increasing imaging depth have to be overcome. The development of new technologies such as miniaturized microscope objectives,<sup>98</sup> video-rate scanning,<sup>28</sup> and longer wavelength excitation<sup>21</sup> will help to facilitate CARS imaging of live animals.

The demonstrated capability of CARS microscopy in *ex vivo* tissue imaging is expected to stir interests in the development of CARS endoscopy for *in vivo* diagnosis. The advantages of label-free chemical imaging of CARS endoscopy are abundantly obvious. First, label-free imaging overcomes the challenges of inefficient diffusion and non-specific targeting of exogenous fluorophores in the complex *in vivo* environment. Second, because CARS does not require electronic resonance, longer excitation wavelengths can be used to minimize multiphoton absorption induced photo-damage. Third, the intrinsic 3D sectioning capability of CARS imaging enables the analysis of spatial organization of bio-structures with molecular details. The

preliminary work on fiber-based CARS imaging<sup>94,99</sup> implied the possibilities of “driving” CARS into hospitals. CARS endoscopy holds great promise for rapid identification of malignancy *in vivo*. For diagnosis of cardiovascular diseases, it is anticipated that CARS endoscopy can be coupled with existing imaging modalities such as optical coherent tomography and intravascular ultrasound on the same catheter-based platform. This combination would create a multimodal imaging tool that is capable of two-dimensional (2D) mapping of morphology with optical coherent tomography and intravascular ultrasound and 3D sub-micrometric imaging of molecular composition with CARS endoscopy.

**ACKNOWLEDGMENTS**

The author acknowledges Haifeng Wang, Li Li, Yan Fu, Terry B. Huff, Thuc Le, Eunah Kang, Han-Wei Wang, and Joshua Robinson for their contributions to the data presented in the paper. The author is grateful for the collaborations with professors Riyi Shi, Kinam Park, Michael Sturek, and Ignacio G. Camarillo in biomedical applications of CARS microscopy. This work was supported by NSF grant 0416785-MCB and NIH grants R21 EB004966, R01 EB007243, and R01 HL078715.

1. J. N. Gannaway and C. J. R. Sheppard, *Opt. Quant. Electron.* **10**, 435 (1978).
2. R. Hellwarth and P. Christensen, *Opt. Commun.* **12**, 318 (1974).
3. M. D. Duncan, J. Reintjes, and T. J. Manuccia, *Opt. Lett.* **7**, 350 (1982).
4. W. Denk, J. H. Strickler, and W. W. Webb, *Science* **248**, 73 (1990).
5. Y. Barad, H. Eisenberg, M. Horowitz, and Y. Silberberg, *Appl. Phys. Lett.* **70**, 922 (1997).
6. A. Zumbusch, G. R. Holtom, and X. S. Xie, *Phys. Rev. Lett.* **82**, 4142 (1999).
7. W. R. Zipfel, R. M. Williams, and W. W. Webb, *Nat. Biotechnol.* **21**, 1369 (2003).
8. P. J. Campagnola and L. M. Loew, *Nat. Biotechnol.* **21**, 1356 (2003).
9. P. D. Maker and R. W. Terhune, *Phys. Rev.* **137**, A801 (1965).
10. R. F. Begley, A. B. Harvey, and R. L. Byer, *Appl. Phys. Lett.* **25**, 387 (1974).
11. Y. R. Shen, *The Principles of Nonlinear Optics* (John Wiley and Sons, New York, 1984).
12. M. D. Levenson and S. S. Kano, *Introduction to Nonlinear Laser Spectroscopy* (Academic Press, San Diego, 1988).
13. S. Mukamel, *Principles of Nonlinear Optical Spectroscopy* (Oxford University Press, New York, 1995).
14. M. D. Levenson and J. J. Song, *Coherent*

*Nonlinear Optics: Recent Advances*, M. S. Feld and V. S. Letokhov, Eds. (Springer-Verlag, Berlin, 1980), p. 293.

15. G. R. Holtom, B. D. Thrall, B.-Y. Chin, H. S. Wiley, and S. D. Colson, *Traffic* **2**, 781 (2001).
16. J. X. Cheng and X. S. Xie, *J. Phys. Chem. B* **108**, 827 (2004).
17. A. Volkmer, *J. Phys. D: Appl. Phys.* **38**, R59 (2005).
18. L. G. Rodriguez, S. J. Lockett, and G. R. Holtom, *Cytometry* **69A**, 779 (2006).
19. M. D. Duncan, *Opt. Comm.* **50**, 307 (1984).
20. M. D. Duncan, J. Reintjes, and T. J. Manuccia, *Opt. Eng.* **24**, 352 (1985).
21. F. Ganikhanov, S. Carrasco, X. S. Xie, M. Katz, W. Seitz, and D. Kopf, *Opt. Lett.* **31**, 1292 (2006).
22. Y. Fu, H. Wang, R. Shi, and J. X. Cheng, *Opt. Exp.* **14**, 3942 (2006).
23. J. X. Cheng, A. Volkmer, L. D. Book, and X. S. Xie, *J. Phys. Chem. B* **105**, 1277 (2001).
24. M. Hashimoto, T. Araki, and S. Kawata, *Opt. Lett.* **25**, 1768 (2000).
25. O. Burkacky, A. Zumbusch, C. Brackmann, and A. Enejder, *Opt. Lett.* **31**, 3656 (2006).
26. A. Volkmer, J. X. Cheng, and X. S. Xie, *Phys. Rev. Lett.* **87**, 023901 (2001).
27. J. X. Cheng, A. Volkmer, and X. S. Xie, *J. Opt. Soc. Am. B* **19**, 1363 (2002).
28. C. L. Evans, E. O. Potma, M. Puoris'haag, D. Côté, C. P. Lin, and S. Xie, *Proc. Natl. Acad. Sci. U.S.A.* **102**, 16807 (2005).
29. T. B. Huff and J. X. Cheng, *J. Microsc.* **225**, 190 (2007).
30. J. X. Cheng, Y. K. Jia, G. Zheng, and X. S. Xie, *Biophys. J.* **83**, 502 (2002).
31. S. A. Akhmanov, A. F. Bunkin, S. G. Ivanov, and N. I. Koroteev, *JETP Lett. (Engl. Transl.)* **25**, 416 (1977).
32. J.-L. Oudar, R. W. Smith, and Y. R. Shen, *Appl. Phys. Lett.* **34**, 758 (1979).
33. A. Laubereau and W. Kaiser, *Rev. Mod. Phys.* **50**, 607 (1978).
34. B. Hudson, W. Hetherington, S. Cramer, I. Chabay, and G. K. Klauminzer, *Proc. Natl. Acad. Sci. U.S.A.* **73**, 3798 (1976).
35. J. R. Andrews, R. M. Hochstrasser, and H. P. Trommsdorff, *Chem. Phys.* **62**, 87 (1981).
36. Y. Yacoby, R. Fitzgibbon, and B. Lax, *J. Appl. Phys.* **51**, 3072 (1980).
37. J. X. Cheng, L. D. Book, and X. S. Xie, *Opt. Lett.* **26**, 1341 (2001).
38. J. X. Cheng, A. Volkmer, L. D. Book, and X. S. Xie, *J. Phys. Chem.* **106**, 8493 (2002).
39. R. Brakel and F. W. Schneider, *Advances in Non-linear Spectroscopy*, R. J. H. Clark and R. E. Hester, Eds. (John Wiley and Sons, New York, 1988), p. 149.
40. A. Volkmer, L. D. Book, and X. S. Xie, *Appl. Phys. Lett.* **80**, 1505 (2002).
41. N. Dudovich, D. Oron, and Y. Silberberg, *Nature (London)* **418**, 512 (2002).
42. D. Oron, N. Dudovich, and Y. Silberberg, *Phys. Rev. Lett.* **90**, 213902 (2003).

43. V. V. Krishnamachari and E. O. Potma, *J. Opt. Soc. Am. A* **24**, 1138 (2007).
44. V. V. Krishnamachari and E. O. Potma, *Chem. Phys.*, paper in press (2007).
45. C. L. Evans, E. O. Potma, and X. S. Xie, *Opt. Lett.* **29**, 2923 (2004).
46. D. L. Marks and S. A. Boppert, *Phys. Rev. Lett.* **92**, 123905 (2004).
47. D. L. Marks, C. Vinegoni, J. S. Bredfeldt, and S. A. Boppert, *Appl. Phys. Lett.* **85**, 5787 (2004).
48. S.-H. Lim, A. G. Caster, and S. R. Leone, *Phys. Rev. A* **72**, 041803 (2005).
49. E. O. Potma, C. L. Evans, and X. S. Xie, *Opt. Lett.* **31**, 241 (2006).
50. T. W. Kee, H. X. Zhao, and M. T. Cicerone, *Opt. Exp.* **14**, 3631 (2006).
51. B. von Vacano, T. Buckup, and M. Motzkus, *Opt. Lett.* **31**, 2495 (2006).
52. S. H. Lim, A. G. Caster, O. Nicolet, and S. R. Leone, *J. Phys. Chem. B* **110**, 5196 (2006).
53. L. Li, H. Wang, and J. X. Cheng, *Biophys. J.* **89**, 3480 (2005).
54. X. Nan, J. X. Cheng, and X. S. Xie, *J. Lipid Res.* **40**, 2202 (2003).
55. X. Nan, E. O. Potma, and X. S. Xie, *Biophys. J.* **91**, 728 (2006).
56. T. T. Le, C. R. Rehner, T. B. Huff, M. B. Nichols, I. G. Camarillo, and J. X. Cheng, *Mol. Imaging*, paper in press. (2007).
57. E. O. Potma and X. S. Xie, *J. Raman Spectrosc.* **34**, 642 (2003).
58. H. Wang, Y. Fu, P. Zickmund, R. Shi, and J. X. Cheng, *Biophys. J.* **89**, 581 (2005).
59. E. Kang, H. Wang, I. K. Kwon, J. Robinson, K. Park, and J. X. Cheng, *Anal. Chem.* **78**, 8036 (2006).
60. F. Ganikhanov, C. L. Evans, B. G. Saar, and X. S. Xie, *Opt. Lett.* **31**, 1872 (2006).
61. Y. Fu, H. Wang, R. Shi, and J. X. Cheng, *Biophys. J.* **92**, 3251 (2007).
62. T. T. Le, I. M. Langohr, M. J. Locker, M. Sturek, and J. X. Cheng, *J. Biomed. Opt.*, paper in press (2007).
63. G. W. H. Wurpel, J. M. Schins, and M. Müller, *Opt. Lett.* **27**, 1093 (2002).
64. T. Hellerer, A. M. K. Enejder, and A. Zumbusch, *Appl. Phys. Lett.* **85**, 25 (2004).
65. K. P. Knutsen, J. C. Johnson, A. E. Miller, P. B. Peterson, and R. J. Saykally, *Chem. Phys. Lett.* **387**, 436 (2004).
66. H. N. Paulsen, K. M. Hilligsoe, J. Thøgersen, S. R. Keiding, and J. J. Larsen, *Opt. Lett.* **28**, 1123 (2003).
67. H. Kano and H. Hamaguchi, *Appl. Phys. Lett.* **85**, 4298 (2004).
68. T. W. Kee and M. T. Cicerone, *Opt. Lett.* **29**, 2701 (2004).
69. G. I. Petrov and V. V. Yakovlev, *Opt. Exp.* **13**, 1299 (2005).
70. E. R. Andresen, H. N. Paulsen, V. Birkedal, J. Thøgersen, and S. R. Keiding, *J. Opt. Soc. Am. B* **22**, 1934 (2005).
71. J. P. Ogilvie, E. Beaurepaire, A. Alexandrou, and M. Joffre, *Opt. Lett.* **31**, 480 (2006).
72. R. Shimada, H. Kano, and H. Hamaguchi, *Opt. Lett.* **31**, 320 (2006).

## focal point

---

73. E. M. Vartiainen, H. A. Rinia, M. Muller, and M. Bonn, *Opt. Exp.* **14**, 3622 (2006).
74. T. H. Tsai, S. P. Tai, W. J. Lee, H. Y. Huang, Y. H. Liao, and C. K. Sun, *Opt. Exp.* **14**, 749 (2006).
75. A. P. Kennedy, J. Sutcliffe, and J. X. Cheng, *Langmuir* **21**, 6478 (2005).
76. J. X. Cheng, S. Pautot, D. A. Weitz, and X. S. Xie, *Proc. Natl. Acad. Sci. U.S.A.* **100**, 9826 (2003).
77. G. W. H. Wurpel and M. Müller, *Chem. Phys. Lett.* **425**, 336 (2006).
78. H. Wang, Y. Fu, and J. X. Cheng, *J. Opt. Soc. Am. B* **24**, 544 (2007).
79. M. Edidin, *Annu. Rev. Biophys. Biomol. Struct.* **32**, 257 (2003).
80. G. W. H. Wurpel, J. M. Schins, and M. Müller, *J. Phys. Chem.* **2004**, 3400 (2004).
81. E. O. Potma and X. S. Xie, *Chem. Phys. Chem.* **6**, 77 (2005).
82. E. O. Potma, W. P. D. Boeij, P. J. M. v. Haastert, and D. A. Wiersma, *Proc. Natl. Acad. Sci. U.S.A.* **98**, 1577 (2001).
83. *Myelin Biology and its Disorders*, R. A. Lazzarini, Ed. (Elsevier Academic Press, San Diego, CA, 2004), vol. 1.
84. Y. Fu, H. Wang, T. B. Huff, R. Shi, and J. X. Cheng, *J. Neurosci. Res.*, paper in press (2007).
85. E. Kang, J. Robinson, K. Park, and J. X. Cheng, *J. Control. Release*, paper in press (2007).
86. Z. S. Galis, *Circ. Res.* **86**, 1 (2000).
87. N. Djaker, P. F. Lenne, D. Marguet, A. Colonna, C. Hadjur, and H. Rigneault, *Nucl. Instrum. Methods Phys. Res., Sect. A* **571**, 177 (2007).
88. W. R. Zipfel, R. M. Williams, R. Christie, A. Y. Nikitin, B. T. Hyman, and W. W. Webb, *Proc. Natl. Acad. Sci. U.S.A.* **100**, 7075 (2003).
89. K. F. Adams, A. Schatzkin, T. B. Harris, V. Kipnis, T. Mouw, R. Ballard-Barbash, A. Hollenbeck, and M. F. Leitzmann, *N. Engl. J. Med.* **355**, 763 (2006).
90. L. F. Van Gaal, I. L. Mertens, and C. E. De Block, *Nature (London)* **444**, 875 (2006).
91. T. Yamaguchi, N. Omatsu, E. Morimoto, H. Nakashima, K. Ueno, T. Tanaka, K. Satouchi, F. Hirose, and T. Osumi, *J. Lipid Res.* **48**, 1078 (2007).
92. L. Li and J. X. Cheng, *Biochemistry* **45**, 11819 (2006).
93. L. Tong, Y. Lu, R. J. Lee, and J. X. Cheng, *J. Phys. Chem. B*, paper in press (2007).
94. H. Wang, T. B. Huff, and J. X. Cheng, *Opt. Lett.* **31**, 1417 (2006).
95. T. W. Koo, S. Chan, and A. A. Berlin, *Opt. Lett.* **30**, 1024 (2005).
96. T. Ichimura, N. Hayazawa, M. Hashimoto, Y. Inouye, and S. Kawata, *Phys. Rev. Lett.* **92**, 220801 (2004).
97. C. Heinrich, S. Bernet, and M. Ritsch-Marte, *New J. Phys.* **8**, 1 (2006).
98. H. Wang, T. B. Huff, Y. Fu, K. Y. Jia, and J. X. Cheng, *Opt. Lett.*, paper in press (2007).
99. F. Légaré, C. L. Evans, F. Ganikhanov, and X. S. Xie, *Opt. Exp.* **14**, 4427 (2006).